Enhancing Rotational Diffusion Using Oscillatory Shear

Brian D. Leahy,[1] Xiang Cheng,[1] Desmond C. Ong,[1] Chekesha Liddell-Watson,[2] and Itai Cohen[1]

[1]*Department of Physics, Cornell University, Ithaca, New York 14853, USA*
[2]*Department of Materials Science and Engineering, Cornell University, Ithaca, New York 14853, USA*
(Received 29 January 2013; published 29 May 2013)

Taylor dispersion—shear-induced enhancement of translational diffusion—is an important phenomenon with applications ranging from pharmacology to geology. Through experiments and simulations, we show that rotational diffusion is also enhanced for anisotropic particles in oscillatory shear. This enhancement arises from variations in the particle's rotation (Jeffery orbit) and depends on the strain amplitude, rate, and particle aspect ratio in a manner that is distinct from the translational diffusion. This separate tunability of translational and rotational diffusion opens the door to new techniques for controlling positions and orientations of suspended anisotropic colloids.

G. I. Taylor [1] was the first to point out that a Brownian particle in a pipe diffuses faster when the suspension is flowing. Qualitatively, this behavior arises because diffusion along the radius of the pipe allows the particle to be advected with the flow at different speeds [1,2]. This effect on translational diffusion is general. As such, Taylor dispersion has become a useful paradigm for understanding diverse phenomena ranging from fluid transport in rock strata [3,4], to nutrient distribution in farm soils [5], to drug delivery control [6], and to the measurement of the diffusion constants of slowly diffusing substances [7,8].

Given the importance of enhanced translational diffusion, we ask whether dispersant orientations are also affected by shear. Colloidal particle orientations are randomized by thermal motion via rotational diffusion [9]. However, the effect of flows on orientational diffusion remains poorly understood. Enhanced translational diffusion under shear results from the particle accessing streamlines with different flow velocities. Similarly, we expect that a particle with access to rotational trajectories with different angular velocities might display enhanced rotational diffusion. Particles with axial symmetry "tumble" with an unsteady rotation in what are known as Jeffery orbits. The orientation of these particles is completely specified by a unit normal $\vec{n}$. For a particle with an effective aspect ratio p in a flow with strain rate $\dot{\gamma}$, the periodic tumbling is described by [10,11]

$$\tan\phi(t) = p\tan\left(\frac{\dot{\gamma}t}{p + 1/p}\right),$$
$$\tan^2\theta = \left[\kappa^2(p\cos^2\phi + 1/p\sin^2\phi)\right]^{-1}, \quad (1)$$

where ϕ is the azimuthal angle from the gradient direction, θ is the polar angle between the vorticity direction and the particle's orientation, and κ^2 is an orbit constant set by the initial conditions. For isotropic particles $p = 1$ and the particle tumbles uniformly. However, if $p \neq 1$, a particle's orientation is advected with different angular velocities

depending on its position in the periodic orbit. Thus, in analogy with results for translational Taylor dispersion, we would expect enhanced rotational diffusion for nonspherical particles under shear.

Here we report experiments and simulations addressing rotational and translational diffusion of colloid dimers under oscillatory shear. We find the rotational diffusion is enhanced and depends on the dimensionless strain rate or Péclet number Pe, effective aspect ratio p, and shear strain γ. Moreover, the dependence of rotational diffusion on these three parameters differs markedly from the translational diffusion. With the advent of new techniques for synthesizing nonspherical particles and their increasing importance in novel materials [12,13], separate tunability of rotations and orientations promises important applications in mixing and self-assembly.

To explore rotational diffusion under shear, we used hollow silica colloidal dimers whose lobes are $\approx 1\ \mu m$ in diameter [14] suspended in an index-matched but density-mismatched 80:20 glycerol:water solution dyed with fluorescein salt. The dimers are slightly elongated, with a length-to-width aspect ratio of 2.5. In addition, we determined the dimer hydrodynamic aspect ratio by fitting 200 measured Jeffery orbits to Eq. (1). We measure a median aspect ratio of 2.3 ± 0.9, consistent with previous predictions and measurements for true dimers [15,16].

Previous studies demonstrated that dense suspensions of rodlike particles under shear display enhanced translational or rotational diffusion, which can arise from many-body hydrodynamic effects [17], collisions [18], or particle-particle interactions [19]. To focus solely on coupling between Brownian motion and shear, we use suspensions at very dilute volume fractions of $\approx 10^{-4}$. Consequently, to obtain statistical power each particle must be tracked for days at a time. While such measurements are challenging due to limitations in apparatus stability, they cleanly eliminate many body effects and clarify the interpretation of our results.

The suspension is loaded in a shear cell consisting of a 4×4 mm silicon wafer positioned above a glass cover slip and held parallel with less than 1 μm variation over the length of the wafer. The gap separation was tuned from 7 to 12 μm in order to vary the strain amplitude. While the plate separation could be set accurately, over the duration of our long experiments we measured that the gap size could drift by up to 20%, which in turn affected the applied strain. The silicon wafer is held stationary, while the glass cover slip is sheared by a piezo controller under oscillatory triangle-wave shear. Our setup mounts on a fast confocal microscope allowing us to accurately image the three-dimensional position and orientation of a colloidal dimer at peak-to-peak shear strains up to $\gamma = 3.4$ and frequencies up to 0.2 Hz.

We image the dimer's position and orientation with a full three-dimensional scan, oversampling in all three directions to increase measurement precision [see Fig. 1(a)]. After accounting for optical distortion [20], we use a custom featuring code to reconstruct the particle voxels [see Fig. 1(b)]. Principal component analysis is used to determine the particle orientation [21]. Using this method we can determine the particle orientation to within $\approx 5°$ as well as locate the particle's position with subpixel

resolution—within 30 nm in the flow x and vorticity z directions, and within 100 nm in the gradient direction y.

Under shear, the dimer's position is advected with the flow, while its orientation tumbles in a Jeffery orbit. Translational and rotational Brownian motion additionally randomize the position and orientation, resulting in a net displacement after each cycle [see Fig. 1(c)]. To track the long-time behavior of the dimer under shear, we take a strobed image at both ends of the triangular cycle [see Figs. 1(d) and 1(e)] and reconstruct its trajectory [22]. From these trajectories we extract the orientational distributions (see Fig. 2). The effective translational diffusion tensor $\mathbf{D}_{\text{eff}}$, and the effective rotational diffusion constant D_{eff}^{r} are extracted using the time correlations:

$$\langle \vec{n}(t) \cdot \vec{n}(t + \Delta t) \rangle = e^{-2D_{\text{eff}}^{r}\Delta t},$$
$$\langle x_i(t)x_j(t + \Delta t) \rangle = 2(D_{\text{eff}}^{T})_{ij}\Delta t, \tag{2}$$

where Δt is an integer number of periods T [see Figs. 3(a) and 3(b)]. While we find that the rotational data in Fig. 3(b) are well fit by a single exponential decay, we note that rotational diffusion is strictly speaking a tensorial quantity that can in principle vary with orientation.

To complement our experimental investigations, we model a colloidal dimer in a shear flow with a Langevin equation. The particle orientation $\vec{n}$ evolves as

$$\frac{d\vec{n}}{dt} = \left(\mathbf{\Omega} \cdot \vec{n} + \frac{p^2 - 1}{p^2 + 1}[\mathbf{E} \cdot \vec{n} - \vec{n}(\vec{n} \cdot \mathbf{E} \cdot \vec{n})]\right)$$
$$+ (2D_0^r)^{1/2}\vec{\Gamma}(t). \tag{3}$$

The first term in the large parentheses describes a uniform rotation due to a shear flow, and the second term accounts
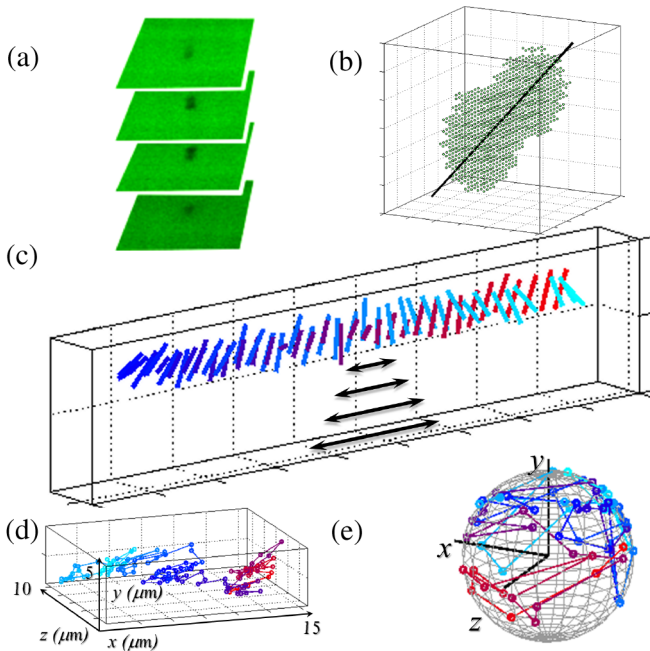

FIG. 1 (color online). (a) Representative confocal microscope images of a dimer. (b) The reconstructed voxels and orientation of the dimer. (c) The reconstructed trajectory of dimer under triangle-wave shear. The flow direction is indicated by arrows. The peak-to-peak strain is $\gamma = 3.4$ and the period $T = 100$ seconds. The dimer's position and orientation are represented by the rod, and the color variation represents the time. In our analysis, we record the dimer position and orientation at the cycle extrema, corresponding to the cyan, blue, and red rods. (d) A trajectory of 250 strobed positions, color coded in time. (e) The corresponding orientations, plotted on the unit sphere.
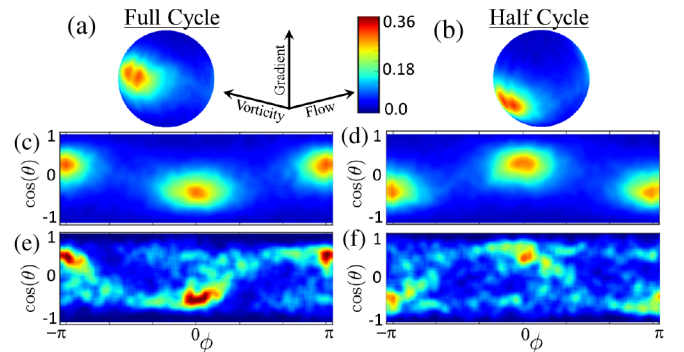

FIG. 2 (color online). (a), (b) Measured orientation distribution from 12 000 simulation cycles at $p = 2.3$, Pe = 600, and $\gamma = 3.4$, plotted on the unit sphere. The distribution oscillates with the flow. Thus different orientations are observed at integer versus half-integer cycles. (c), (d) The same distribution as in (a) and (b), but plotted with an equiareal mapping where θ is the polar angle measured from the gradient direction, and ϕ is the azimuthal angle measured from the flow direction. (e), (f) The orientation distribution from experiment, separated by full (e) versus half (f) cycles, measured at the same Pe, γ. All images share the same color scale.
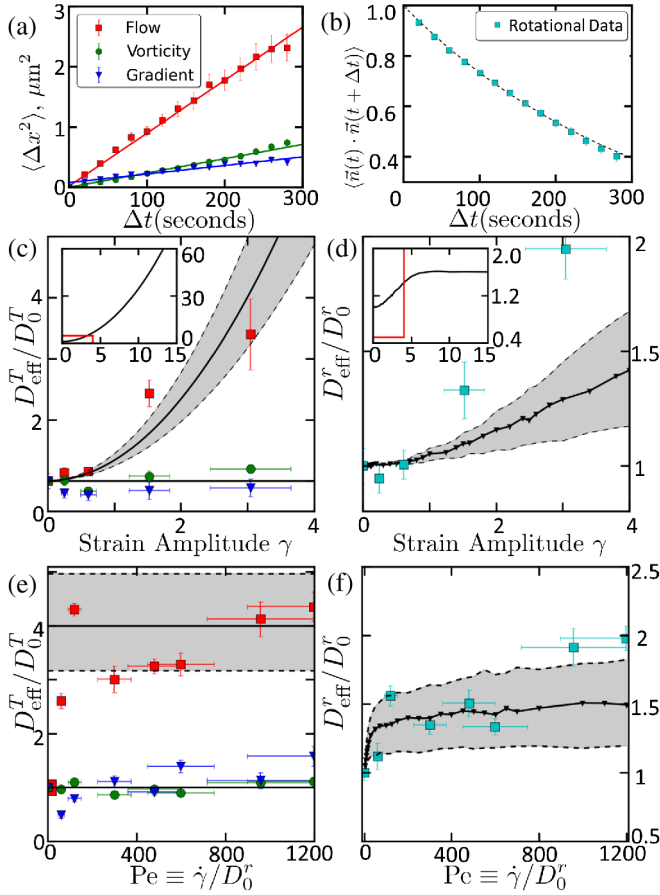
FIG. 3 (color online).   (a) Measured mean-square displacement along flow (red squares), vorticity (green circles), and gradient (blue triangles) directions. (b) Measured correlation of the corresponding orientations. (c) Normalized translational diffusion $\mathbf{D}_{\text{eff}}^T/D_0^T$, along all three axes versus γ at fixed $\text{Pe} = 80$. Symbols correspond to measurements while the black lines correspond to predicted values [Eq. (4)]. The gray band indicates the effects of experimental uncertainty in γ on the prediction. Inset: The predicted diffusion along the flow direction for $0 < \gamma < 15$. Red box illustrates range in main panel. (d) D_{eff}^r/D_0^r for the same data set as (c), as measured from experiment (cyan squares) and simulation at $p = 2.3$ (black points). Shaded band indicates the effect of experimental uncertainty in aspect ratio. Inset: Simulated rotational diffusion for $0 < \gamma < 15$. Red box illustrates range in main panel. (e), (f) Translational (e) and rotational (f) diffusion at constant $\gamma = 3.4$ and varying Pe. Overlaid in black lines are the expected values from theory (c) and simulation (d).

for the effects arising from particle shape and orientation relative to the imposed shear strain [10]. The final term on the right hand side accounts for rotational Brownian motion. Here D_0^r is the rotational diffusion constant of the particle and $\vec{\Gamma}$ is a diffusive white-noise term. $\mathbf{\Omega}$ is the vorticity tensor and $\mathbf{E}$ is the rate-of-strain tensor for triangle-wave oscillatory shear: $\mathbf{\Omega}_{ij} = 1/2(\partial_i u_j - \partial_j u_i)$, $\mathbf{E}_{ij} = 1/2(\partial_i u_j + \partial_j u_i)$.

Our experiment consists of suspensions of sedimenting spheroids in a shear flow bounded by rigid surfaces,

whereas our simulation models the rotation of a single spheroid in an infinite fluid. While our experiment minimizes interparticle hydrodynamic interactions [17,23–25] by using extremely dilute volume fractions, because of the geometry of the experiment we cannot avoid interactions with the wall [26,27]. Nevertheless, we find similar behavior between our experiments and simulations, despite the fact that the walls considerably influence the translational dynamics. We posit that the reason for this agreement is that, as simulations have shown, the wall's effect is only at the few percent level on the Jeffery orbits [26], which is what ultimately affects the rotational diffusion.

Three dimensionless parameters control the particle's distribution and diffusivities: the aspect ratio p, the dimensionless strain rate or Péclet number $\text{Pe} = \dot{\gamma}/D_0^r$, and the peak-to-peak strain amplitude $\gamma = \dot{\gamma}T/2$ [Eq. (3)]. Previous works [28] have shown that Eq. (3) leads to an inhomogeneous steady-state distribution of particle orientations under continuous shear. In contrast, our experiments and simulations for oscillatory shear show that the orientational distribution oscillates with the flow [Figs. 2(b) and 2(d) versus Figs. 2(c) and 2(e)]. While the distributions show the $\vec{n} \rightarrow -\vec{n}$ symmetry required by Eq. (3), they are not symmetric about either the gradient or flow axes separately (see the Supplemental Material [29]). At low Pe, γ, or near $p = 1$, the orientational distribution becomes isotropic. Interestingly, increasing Pe at fixed γ strengthens the alignment, whereas increasing γ at fixed Pe both strengthens the alignment and alters its direction. We find excellent agreement between simulations and experiments. Moreover, at high amplitude and high Pe the simulated distributions approach previous calculations for rods under continuous shear [28].

In addition to distributions, we simultaneously measure the particle's rotational and translational diffusion after an integer number of cycles. We find the particle's translational [19,30] and rotational motions are well fit by diffusive trajectories of Eq. (2). The translational mean-square displacement, shown in Fig. 3(a), increases linearly with time while the time-correlation of particle orientations, shown in Fig. 3(b), exponentially decays. From these curves we extract effective diffusion constants, which depend on the dimensionless parameters Pe, γ, and p.

The experimental data in Fig. 3(c) show the translational diffusion along the flow direction $(D_{\text{eff}}^T)_{xx}$ increasing with γ. $(D_{\text{eff}}^T)_{xx}$ ranges from its equilibrium value at $\gamma = 0$ to ≈ 3.5 times its equilibrium value at $\gamma = 3$. In contrast, the diffusion constants along the gradient and vorticity directions $(D_{\text{eff}}^T)_{yy}$ and $(D_{\text{eff}}^T)_{zz}$ remain at the equilibrium value. Theory predicts that for spherical particles in triangle-wave shear the diffusivity is [30]

$$\langle x^2 \rangle = 2D_x t + \frac{2}{3}D_y \gamma^2 t \quad \langle y^2 \rangle = 2D_y t \quad \langle z^2 \rangle = 2D_z t, \quad (4)$$

where x, y, and z are the flow, gradient, and vorticity directions and t is taken at integer multiples of the cycle period. Clearly, an anisotropic particle has different diffusivities along its different axes [31,32]. Since the particle's orientation couples to the flow, D_x, D_y, and D_z in Eq. (4) will depend on the applied shear flow. Building on results for continuous shear [33], however, we calculate this change to be at the few percent level in our experiments. We thus compare our data with Eq. 4 in Fig. 3 using equilibrium values for D_x, D_y, D_z. We find excellent agreement between theory (black lines) and experiments (data points) for all the effective diffusion constants. As predicted, only $(D_{\text{eff}}^T)_{xx}$ increases with γ. As shown in the inset of Fig. 3 the effective diffusion along the flow direction increases quadratically with γ indefinitely.

Since at fixed γ $\mathbf{D}_{\text{eff}}^T$ depends on Pe only through D_x, D_y, D_z, we predict an enhanced $(D_{\text{eff}}^T)_{xx}$ even as Pe $\rightarrow 0$ and no measurable dependence of D_{eff}^T on Pe. As expected, we observe that $(D_{\text{eff}}^T)_{yy}$ and $(D_{\text{eff}}^T)_{zz}$ remain constant while $(D_{\text{eff}}^T)_{xx}$ is significantly enhanced even at the lowest Pe measured [see Fig. 3(e)]. However, there is a weak trend in the $(D_{\text{eff}}^T)_{xx}$ data. We attribute this trend to experimental effects from fluctuations in the shear cell gap (gray band) and gravitational settling that can affect data at low Pe [29].

We find that D_{eff}^r is also enhanced by shear, nearly doubling by $\gamma = 3$ [see Fig. 3(d)]. A similar trend is observed in our simulations (black line; gray band accounts for uncertainty in p). However, simulations at larger γ than those accessible in experiments show that D_{eff}^r saturates at a value that depends on Pe and p [see the inset of Fig. 3(d)]. Because Jeffery orbits are periodic with strain, after the orientation has completed half a period [$\gamma = \pi(p + 1/p)$] no new rotational dynamics appear. Since larger strain does not provide access to new changes in the streamlines, the rotational diffusion saturates. In contrast, the translational diffusion increases indefinitely, as there is no strain scale for translations.

The Pe dependence of D_{eff}^r contrasts with translational diffusion. While $(D_{\text{eff}}^T)_{xx}$ remains enhanced at low Pe, in both experiment and simulation D_{eff}^r increases continuously with Pe [see Fig. 3(f)]. Our simulations also suggest that for large Pe D_{eff}^r still increases, albeit slowly [29].

A more complete map of the dependence of D_{eff}^r on Pe and γ for $p = 2.8$ is shown in Fig. 4(a). This figure summarises 778 simulations of D_{eff}^r in the range $0 < \gamma < 30$ and $0 < \text{Pe} < 1400$. The heat maps show that both trends—D_{eff}^r increasing slowly with Pe and saturating at high γ—are general over a large range of parameters. In addition, they illustrate two unexpected trends. First, the slight slopes observed for the contours of D_{eff}^r indicate that the dependence on Pe and γ is coupled. Second, we find multiple resonances in D_{eff}^r with increasing γ, visible as the dark red "bumps" at high Pe in Fig. 4(a) and the peaks in Fig. 4(c). These oscillations result from the Jeffery orbit periodicity. Particle rotation under triangle-wave shear
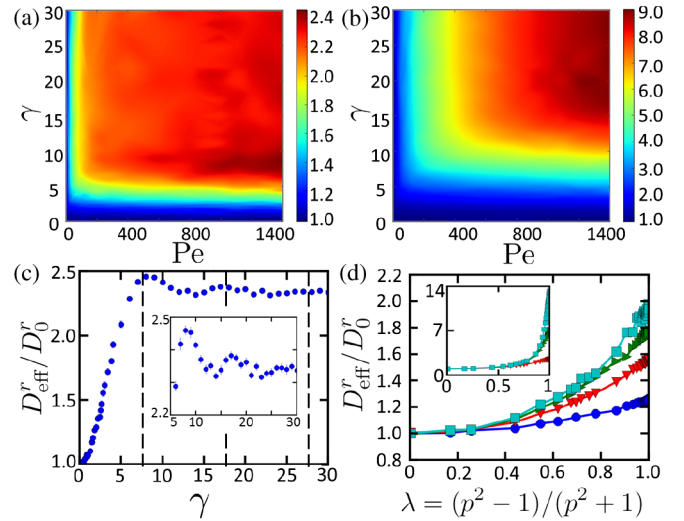

FIG. 4 (color online). D_{eff}^r/D_0^r, plotted against both Pe and γ at $p = 2.83$ (a) and $p = 7.0$ (b). (c) Data from (a) at Pe $= 1400$ demonstrating oscillations in D_{eff}^r with γ. (d) D_{eff}^r/D_0^r versus $\lambda = (p^2 - 1)/(p^2 + 1)$, taken at fixed $\gamma = 2.83$ and at four separate Pe: 10 (blue circles), 40 (red vertical triangles), 289 (green horizontal triangles), and 1000 (cyan squares). Inset: D_{eff}^r/D_0^r versus λ at Pe $= 10, 40, 1000$ and $\gamma = 15$.

maps onto rotation under continuous shear when γ corresponds to an integer number of half Jeffery orbits [distance between vertical dashed lines in Fig. 4(c)].

While it is known that increasing aspect ratio can at most vary translational diffusion anisotropy by a factor of 2 for rods in bulk fluids [34], here we find a much stronger dependence of the rotational diffusion on aspect ratio. Although it is difficult to alter the aspect ratio in experiments, we can examine the dependence of D_{eff}^r on p in simulation. To this end, we evaluated D_{eff}^r at 537 different γ and Pe values and at fixed $p = 7.0$ [see Fig. 4(b)]. At large Pe the rotational diffusion again saturates when $\gamma \sim \pi(p + 1/p)$. However, while D_{eff}^r at $p = 2.83$ was enhanced by 2.4, we find that D_{eff}^r at $p = 7$ is enhanced by a factor of 9. The general trends in the data for the dependence of D_{eff}^r on p can be examined by plotting D_{eff}^r versus the Jeffery coefficient $\lambda = (p^2 - 1)/(p^2 + 1)$ at fixed Pe and γ [see Fig. 4(d)]. We find that D_{eff}^r remains finite as $p \rightarrow \infty$. For $\gamma = 2.8$ this value is roughly 2 at Pe $= 1000$ [see the cyan squares, in the main panel of Fig. 4(d)] whereas for $\gamma = 15$ this value increases to 14 at Pe $= 1000$ [see the inset of Fig. 4(d)]. Finally, for all simulated Pe and γ, we find no enhanced diffusion in the limit of spherical particles and uniform rotation ($p \rightarrow 1$). Just as enhanced diffusion due to Taylor dispersion requires access to a gradient in the real-space streamlines, enhanced rotational diffusion requires access to nonuniform rotational trajectories.

Overall, the diffusion of a colloidal dimer shows a complex dependence on the shear flow and the particle aspect ratio. Simply by changing the applied shear, the

rotational diffusion of a colloidal particle can be tuned absolutely and relative to the translational diffusion. In particular, by changing γ the translational diffusion increases indefinitely, whereas the rotational diffusion saturates. This separate tunability of orientations and positions opens the door to new techniques for manipulating self-assembly, particle separation, and suspension rheology. Moreover, the formulation of these results extends to two and even three axis shear flows, allowing an additional handle for manipulating particle orientations and positions. Further measurements with larger data sets may be able to look for anisotropy in the rotational diffusion. Nearly 60 years after Taylor originally showed that translational diffusion could be enhanced by flow, new techniques in particle synthesis and measurement of orientational trajectories show that these general principles can be extended to rotational diffusion.

[1] G. Taylor, Proc. R. Soc. A **219,** 186 (1953).
[2] R. Aris, Proc. R. Soc. A **235,** 67 (1956).
[3] C. I. Steefel and K. Maher, Rev. Mineral. Geochem. **70,** 485 (2009).
[4] A. Boustani and B. B. Maini, J. Can. Petrol. Technol. **40,** 68 (2001).
[5] E. Bresler and G. Dagan, Soil Sci. Soc. Am. J. **43,** 467 (1979).
[6] M. S. Fallon, B. A. Howell, and A. Chauhan, Math. Med. Biol. **26,** 263 (2009).
[7] A. Alizadeh, C. A. N. de Castro, and W. A. Wakeham, Int. J. Thermophys. **1,** 243 (1980).
[8] M. S. Bello, R. Rezzon, and P. G. Righetti, Science **266,** 773 (1994).
[9] A. Einstein, *Investigations on the Theory of the Brownian Movement* (Dover, New York, 1956).
[10] G. B. Jeffery, Proc. R. Soc. A **102,** 161 (1922).
[11] F. P. Bretherton, J. Fluid Mech. **14,** 284 (1962).
[12] R. Chaudhuri and S. Paria, Chem. Rev. **112,** 2373 (2012).
[13] S. C. Glotzer and M. J. Solomon, Nat. Mater. **6,** 557 (2007).
[14] S. H. Lee, S. J. Gerbode, B. S. John, A. K. Wolfgang, F. A. Escobedo, I. Cohen, and C. M. Liddell, J. Mater. Chem. **18,** 4912 (2008).
[15] D. Velegol and J. L. Anderson, Langmuir **12,** 675 (1996).
[16] T. G. M. van de Ven and S. G. Mason, J. Colloid Interface Sci. **57,** 517 (1976).
[17] M. Rahnama, D. L. Koch, and E. S. G. Shaqfeh, Phys. Fluids **7,** 487 (1995).
[18] A. Franceschini, E. Filippidi, E. Guazzelli, and D. J. Pine, Phys. Rev. Lett. **107,** 250603 (2011).
[19] X. Qiu, H. D. Ou-Yang, D. J. Pine, and P. M. Chaikin, Phys. Rev. Lett. **61,** 2554 (1988).
[20] S. Hell, G. Reiner, C. Cremer, and E. H. K. Stelzer, J. Microsc. **169,** 391 (1993).
[21] Code is available online at http://cohengroup.ccmr.cornell.edu.
[22] J. C. Crocker and D. G. Grier, J. Colloid Interface Sci. **179,** 298 (1996).
[23] P. T. Underhill, J. P. Hernandez-Ortiz, and M. D. Graham, Phys. Rev. Lett. **100,** 248101 (2008).
[24] A. Acrivos, G. K. Batchelor, E. J. Hinch, D. L. Koch, and R. Mauri, J. Fluid Mech. **240,** 651 (1992).
[25] E. S. G. Shaqfeh and G. H. Fredrickson, Phys. Fluids A **2,** 7 (1990).
[26] C. Pozrikidis, J. Fluid Mech. **541,** 105 (2005).
[27] C. A. Stover and C. Cohen, Rheol. Acta **29,** 192 (1990).
[28] E. J. Hinch and L. G. Leal, J. Fluid Mech. **52,** 683 (1972).
[29] See Supplemental Material at http://link.aps.org/supplemental/10.1103/PhysRevLett.110.228301 for details about the experimental setup and additional data, including movies of the orientational distributions over a range of shear parameters and enhanced rotational diffusion as a function of aspect ratio.
[30] D. T. Leighton, Physicochemical hydrodynamics : PCH **11,** 377 (1989).
[31] Y. Han, A. M. Alsayed, M. Nobili, J. Zhang, T. C. Lubensky, and A. G. Yodh, Science **314,** 626 (2006).
[32] F. Perrin, J. Phys. Radium **5,** 497 (1934).
[33] I. Frankel and H. Brenner, J. Fluid Mech. **255,** 129 (1993).
[34] H. Lamb, *Hydrodynamics* (Dover, New York, 1932).